International Journal of Plasticity 28 (2012) 70–87

Contents lists available at ScienceDirect

International Journal of Plasticity

journal homepage: www.elsevier.com/locate/ijplas

Wedge indentation into elastic–plastic single crystals. 2: Simulations for face-centered cubic crystals

Yuki Saito, Muin S. Oztop, Jeffrey W. Kysar *

Department of Mechanical Engineering, Columbia University, New York, NY 10027, United States

ARTICLE INFO

Article history:
Received 19 October 2010
Received in final revised form 23 May 2011
Available online 15 June 2011

Keywords:
Indentation
Single crystal plasticity
Asymptotic fields
Kink-shear
Glide-shear

ABSTRACT

The asymptotic stress and deformation fields associated with the contact point singularity of a nearly-flat wedge indenter impinging on a specially-oriented single face-centered cubic crystal are derived analytically in a companion paper. In order to investigate the extent of the asymptotic fields, the indentation process is simulated numerically using single crystal plasticity. The quasistatically translating asymptotic fields consist of four angular elastic sectors separated by plastically deforming sector boundaries, as predicted in the companion paper. The asymptotic stress distributions are in accord with the analytical predictions. In addition, simulations are performed for a wedge indenter with a 90° included angle in order to investigate the consequences of finite deformation and finite lattice rotation. Several salient features of the deformation field for the nearly-flat indenter persist in the deformation field for the 90° wedge indenter. The existence of the salient features is validated by comparison to experimental measurements of the lower bound on geometrically necessary dislocation (GND) densities.

1. Introduction

Indentation is a common method to characterize the mechanical properties of a material. Proper interpretation of indentation experiments requires a detailed understanding of the stress and deformation fields in the material under the indenter. The deformation fields are, in general, highly complex with a three-dimensional character and large rotations and strains induced by multiple deformation mechanisms (e.g. both elastic and plastic). The deformation fields at the point where the indenter loses contact with the underlying material are especially severe. There is a well-known analogy (Prandtl, 1920) between a flat punch and a stationary crack, so it is apparent that the stress and deformation fields are singular at these points. Therefore, in the context of indentation, such a point will be referred to as a *contact point singularity*. For indenters that are not flat punches, the contact point singularity propagates along the surface of the material during indentation. Thus, the proper analog of a contact point singularity of a non-flat indenter is a quasistatically *closing* crack tip, which provides a framework for detailed analysis of the contact point singularity.

The singular fields associated with crack tips have been studied extensively for many different material classes. In the context of an elastic–plastic material, an approximation of the constitutive response as being elastic, ideally-plastic simplifies the set of governing equations sufficiently to allow the derivation of analytical solutions for the stress and deformation fields. While idealized, these stress and deformation fields serve as a baseline against which fields from numerical analyses that incorporate more realistic constitutive relations can be compared.

Nanoindentation often induces deformation into individual, or at most a few grains, of a material so it is necessary to consider the anisotropic mechanical constitutive behavior for proper interpretation of the results. This motivated Kysar et al.

* Corresponding author.
E-mail address: jk2079@columbia.edu (J.W. Kysar).

0749-6419/$ - see front matter © 2011 Elsevier Ltd. All rights reserved.
doi:10.1016/j.ijplas.2011.05.013

(2010) to study plastic deformation induced experimentally in a single face-centered crystal of nickel due to wedge indentation with a 90° included angle. The orientation of the crystal relative to the wedge indenter was chosen such that the deformation and stress fields were two-dimensional to within experimental accuracy. The lattice rotation associated with the induced plastic deformation was measured with a 3 μm spatial resolution using Orientation Imaging Microscopy (OIM) based upon automated Electron Backscatter Diffraction (EBSD). The spatially-resolved lower bound of the total density of geometrically necessary dislocations (GNDs) was determined from the Nye dislocation density tensor based upon calculation from the two-dimensional lattice rotation. The experimental results strongly suggest that plastic deformation in the region of the contact point singularities shares characteristics with asymptotic fields associated with crack tips in single crystals in the sense that GND density structures exist along special crystallographic directions that emanate from the contact point singularity.

In order to investigate the detailed deformation state near a contact point singularity associated with indentation into a single crystal, Saito and Kysar (2011)—in a companion paper—considered a nearly-flat wedge indenter as it penetrates the surface of a single crystal so that a two-dimensional deformation state is induced. A nearly-flat wedge is assumed in the analysis so that the change of lattice orientation due to rotation of the crystal lattice is negligible. At first glance, there is no reason to think that the asymptotic fields under the contact point singularities of a nearly-flat wedge should be any different than those under a flat punch. However, Drugan and Rice (1984) showed there to be a restriction on stress discontinuities across quasistatically moving surfaces within a general class of elastic–plastic metals. Rice (1973, 1987) demonstrated that for special orientations of face-centered cubic (FCC) and body-centered cubic (BCC) crystals, the asymptotic fields associated with a stationary contact point singularity are expected to have interior surfaces across which the stresses change discontinuously. Thus the asymptotic fields associated with a quasistatically propagating contact point singularity must be different than the stationary case in order to ensure that stress discontinuities do not exist (Rice, 1987).

Asymptotic fields near contact point singularities consist of angular sectors of material within which the deformation is either instantaneously elastic or plastic. The boundaries between the angular sectors are rays that emanate from the singular point that are limited to lie either parallel to or perpendicular to the effective in-plane slip systems that exist in the specially-oriented crystals used in the analysis. For the case of a flat punch impinging on single crystals for which the contact point singularity remains stationary, Rice (1973, 1987) predicts the asymptotic fields in the FCC orientation to consist entirely of plastic angular sectors with plastically-deforming sector boundaries across which the stress state changes discontinuously. For the case of a nearly-flat wedge indenter for which the contact point singularity translates quasistatically along the material surface, Saito and Kysar (2011) predict the asymptotic fields in the FCC crystal to consist entirely of elastic angular sectors separated by plastically-deforming sector boundaries across which the stress state changes continuously. Interestingly, the angular positions of the sector boundaries are the same for both cases.

Rice (1987) demonstrated that the form of the asymptotic fields in single crystals depends upon whether the singularity is stationary or moving quasistatically. The form of the asymptotic fields may also be sensitive to the elastic properties of the material such as Poisson's ratio (Zhang and Huang, 1994; Huang, 1995). In addition, the form of the asymptotic fields may be sensitive to the ability or inability of certain dislocation structures that lead to the formation of kink-like shear (Drugan, 2001). Finally, since the analytical formulation to derive the asymptotic fields is a generalization of standard anisotropic slip-line theory, the analytical solutions are generally not unique and finite lattice rotation is not taken into account. Thus, numerical methods are complementary to the analytical methods for analysis of the asymptotic stress and deformation fields.

The main purpose of this paper is to investigate the asymptotic fields associated with the contact point singularity of a nearly-flat wedge indenter impinging onto an elastic, ideally-plastic single crystal and to compare the results to the analytical solutions by Saito and Kysar (2011). A nearly-flat wedge indenter is assumed so that the effects of crystal lattice rotation can be neglected. While the analytical and the numerical solutions both assume highly idealized elastic, ideally-plastic constitutive relationships, the resulting stress and deformation fields serve as a point of reference for further analyses that incorporate more realistic constitutive relations. In addition, we also report the results of single crystal plasticity simulations of indentation with a 90° wedge indenter. In this way the effects of finite deformations and lattice rotations caused by the 90° wedge indenter can be determined by comparison with the results for the nearly-flat wedge. In addition, the results can be compared to experiments by Kysar et al. (2010) of indentation into a nickel single crystal with a 90° wedge indenter.

This paper is organized in the following way. We briefly review in Section 2 the analytical predictions of the asymptotic stress and deformation fields associated with a quasistatically moving contact point singularity in a specially-oriented FCC single crystal in the limit of a nearly-flat indenter. Sections 3 and 4 discuss the basics of single crystal plasticity and the finite element implementation, respectively, used in the simulations. The results of the single crystal plasticity finite element simulation of indentation with the nearly-flat indenter are presented in Section 5 and are compared to the analytical predictions of Saito and Kysar (2011). Then, Section 6 presents the results of single crystal finite element simulations of indentation with a 90° wedge and compares them to both the nearly-flat wedge simulation as well as experiments by Kysar et al. (2010). Finally, the conclusions are discussed in Section 7.

2. Analytical solution for nearly-flat wedge indentation in single crystal

Single crystals exhibit anisotropic behavior when deformed plastically due to the fact that plastic deformation occurs by the creation and motion of dislocations within the crystal on discrete crystallographic planes (with unit normal $\boldsymbol{n}$) on which

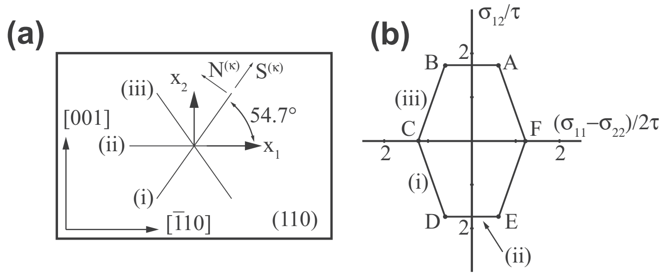

Fig. 1. Effective in-plane plastic slip systems of FCC crystal: (a) orientations of effective slips systems relative to external surface of indented crystal; and, (b) plastic yield surface associated with in-plane deformation, where the effective in-plane slip system associated with each pair of parallel sides of the yield surface is indicated.

dislocations exist and in discrete directions (denoted by unit vector $\boldsymbol{s}$) in the planes in which dislocations move. Together, the unit vectors $\boldsymbol{n}$ and $\boldsymbol{s}$ define a slip system. For a rate independent material, plastic deformation occurs on a specific slip system when a resolved shear stress on the slip plane in the direction of slip reaches a critical value. This is expressed for the κth slip system as

$$s_j^{(\kappa)}\sigma_{ij}n_i^{(\kappa)} = \pm\tau^{(\kappa)}, \tag{1}$$

where σ_{ij} is the applied Cauchy stress tensor and $\tau^{(\kappa)}$ is the experimentally determined critical resolved shear stress of the slip system. (N.B The summation convention is followed for repeating indices, but no summation is performed for any index in parentheses.) Generally, there exist several slip systems depending on the crystal type. An FCC crystal has 12 slip systems with slip planes {111} and slip directions $\langle 110\rangle$, where {111} corresponds to the family of slip planes $\boldsymbol{n}$, and $\langle 110\rangle$ corresponds to the family of slip directions $\boldsymbol{s}$.

Rice (1987) showed that if a line loading is applied parallel to the [110] direction in an FCC crystal, plane deformation conditions are achieved on the corresponding (110) plane with three effective in-plane slip systems. These effective in-plane slip systems will be referred to as slip system (i)–(iii), respectively as detailed in Fig. 1a, where each in-plane slip system has an effective slip plane unit normal, $\mathbf{N}^{(\kappa)}$, and effective unit slip direction, $\mathbf{S}^{(\kappa)}$, that both lie in the (110) plane. Slip system (i) is oriented at an in-plane angle of $\phi_1 = \tan^{-1}\left(\sqrt{2}\right) = 54.7^\circ$, slip system (ii) at $\phi_2 = 0^\circ$, and slip system (iii) at $\phi_3 = -\tan^{-1}\left(\sqrt{2}\right) = -54.7^\circ$ counterclockwise relative to the $[\bar{1}10]$ direction. The plastic yield surface associated with the in-plane deformation state is shown in Fig. 1b. As discussed in detail elsewhere (Rice, 1987; Kysar et al., 2005), the construction of the yield surface follows directly from Eq. (1).

A schematic representation of the system under consideration is shown in Fig. 2a, where a wedge indenter impinges on a single crystal with three effective in-plane slip systems that have a reflection symmetry about the vertical line that passes through the center of the indented region. The center of the indented region represents an antisymmetry boundary[1] so it is necessary to model only one-half the domain, in this case the right half. We will model the indentation process numerically assuming a nearly-flat wedge with an included angle slightly less than 180° in order to compare the results to analytical calculations from the companion paper (Saito and Kysar, 2011). In addition, we numerically model experiments by Kysar et al. (2010) of the indentation due to a wedge indenter with an included angle of 90° to gain insight into how the deformation fields differ from those of the nearly-flat wedge as a consequence of finite lattice rotation.

For the nearly-flat wedge, we will focus attention on the structure of the asymptotic fields associated with the contact point singularity shown schematically as point **O** in Fig. 2b, which gives a detailed view of the region near the contact point singularity on the right half of the domain. The contact point singularity translates to the right as the indentation process proceeds. The Saito and Kysar (2011) derivation assumes isotropic elasticity and accounts for the fact that stress discontinuities cannot occur in the elastic, ideally-plastic single crystal as the contact point singularity propagates quasistatically; however discontinuities of velocity are admissible in the fields. The angular distribution of the stress components within individual elastic sectors was derived by Drugan et al. (1982) and Drugan (2001). The boundary conditions assume frictionless contact between the indenter and the crystal so that $\sigma_{12} = 0$ and $\sigma_{22} < 0$ on $\theta = -180^\circ$ in Fig. 2b and traction-free conditions ahead of the propagating contact point singularity so that $\sigma_{12} = \sigma_{22} = 0$ on $\theta = 0^\circ$. Full details of the motivation and derivation of the asymptotic fields are in the companion paper (Saito and Kysar, 2011).

The structure of the asymptotic field suggested by the analytical predictions for an FCC crystal is shown in Fig. 2b. The asymptotic field consists of angular sectors centered at the contact point singularity within which the material response is instantaneously elastic; these are denoted as elastic sectors. The material response at the boundaries between the elastic sectors, on the other hand, is instantaneously plastic. The stress state for the FCC case valid for $-180^\circ \leqslant \theta \leqslant 0$ is

[1] We adopt the term *antisymmetric* to describe the lattice rotation field that, according to measurements by Kysar et al. (2010), is equal in magnitude but opposite in sign on the two sides of the antisymmetry boundary.

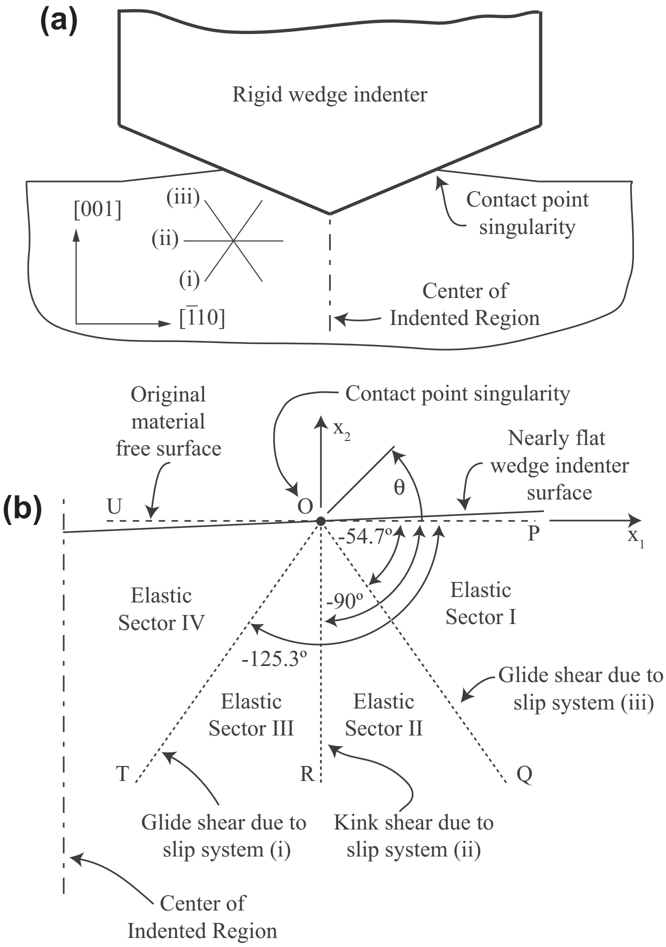

Fig. 2. Wedge indentation into single FCC crystal: (a) orientations of effective slips systems; and, (b) predicted asymptotic deformation field under the contact point singularity.

$$\frac{\sigma_{11}-\sigma_{22}}{2\tau}=\frac{\sqrt{3}}{2}\sin 2\theta, \tag{2a}$$

$$\frac{\sigma_{11}+\sigma_{22}}{2\tau}=\sqrt{3}\theta, \tag{2b}$$

$$\frac{\sigma_{12}}{\tau}=\frac{\sqrt{3}}{2}(1-\cos 2\theta). \tag{2c}$$

The details of the asymptotic solution are plotted in Fig. 3, where the stress trajectory relative to the yield surface in stress space is shown in Fig. 3a and the angular variation of the individual stress components is shown in Fig. 3b. At $\theta = 0°$, the stress is at the origin of the stress space. The trajectory then proceeds clockwise in a circle in stress space as θ decreases from 0° to $-180°$. In the process, the stress trajectory meets the yield surface side (cf. Fig. 1b) associated with slip system (iii) at $\theta = -54.7°$. Since this coincides with the $\mathbf{S}^{(3)}$ that emanates from the contact point singularity (i.e. line **OQ** in Fig. 2b), plastic deformation is induced on slip system (iii) in a glide sense (Rice, 1987). Similarly, the stress trajectory meets the yield surface side associated with slip system (ii) at $\theta = -90°$; since this coincides with the $\mathbf{N}^{(3)}$ that emanates from the contact point singularity (i.e. line **OR**), plastic deformation is induced on slip system (ii) in a kink sense (Rice, 1987). Similarly, a glide shear deformation is induced on slip system (i) on line **OT**.

3. Single crystal plasticity

We now discuss the details of the finite element model simulation of the deformation around a contact point singularity in an FCC single crystals. One simulation will be for the limiting case of a nearly-flat wedge indentation and another will be for a 90° wedge indentation.

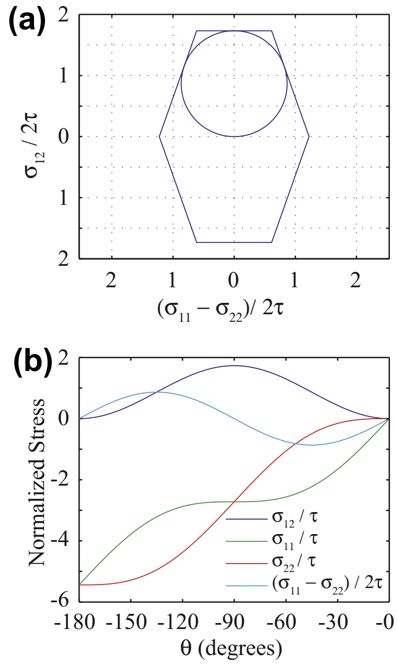

Fig. 3. Asymptotic stress field around contact point singularity for nearly-flat wedge in FCC single crystal: (a) trajectory in stress space; and, (b) angular variation of individual stress components.

3.1. Kinematics and constitutive relationships and numerical algorithm

The study of single crystal plasticity initiated with Taylor and Elam (1923). The kinematics and constitutive relationships of single crystal plasticity are well established (Hill, 1966; Rice, 1971; Hill and Rice, 1972; Havner, 1972; Havner, 1973; Hill and Havner, 1982), as reviewed in Havner (1992). For a general elastic–plastic material under conditions of an infinitesimal deformation gradient, the elastic strain rate and the plastic strain rate sum to the total strain rate is given by

$$\dot{\varepsilon}_{ij} = \dot{\varepsilon}^{e}_{ij} + \dot{\varepsilon}^{p}_{ij}, \tag{3}$$

where superposed dots on the variables refer to differentiation with respect to time. The Schmid factor of the κth slip system is

$$\mu^{(\kappa)}_{ij} = \frac{1}{2}\left(s^{(\kappa)}_i n^{(\kappa)}_j + s^{(\kappa)}_j n^{(\kappa)}_i\right), \tag{4}$$

where $\boldsymbol{n}^{(\kappa)}$ and $\boldsymbol{s}^{(\kappa)}$ denote slip normal and slip direction, respectively, on the κ^{th} slip system. The resolved shear stress on the κth slip system, $\varsigma^{(\kappa)}$, is calculated, from the Cauchy stress tensor σ_{ij} as

$$\varsigma^{(\kappa)} = \sigma_{ij}\mu^{(\kappa)}_{ij}. \tag{5}$$

The plastic strain rate is calculated by summing the contribution of plastic slip rate over all N slip systems as

$$\dot{\varepsilon}^{p}_{ij} = \sum_{\kappa=1}^{N} \mu^{(\kappa)}_{ij}\dot{\gamma}^{(\kappa)}, \tag{6}$$

where $\gamma^{(\alpha)}$ is the plastic slip on the κth slip system. The stress rate $\dot{\sigma}_{ij}$ is related to the elastic strain rate as

$$\dot{\sigma}_{ij} = L_{ijkl}\dot{\varepsilon}^{e}_{kl} = L_{ijkl}\left(\dot{\varepsilon}_{kl} - \dot{\varepsilon}^{p}_{kl}\right), \tag{7}$$

where L_{ijkl} is the elastic moduli tensor having the symmetry $L_{ijkl} = L_{jikl} = L_{ijlk} = L_{klij}$, due to stress tensor symmetry, strain tensor symmetry, and the existence of an elastic potential energy. A viscoplastic (i.e. rate-dependent) constitutive formulation in the form of a power-law expression (Hutchinson, 1976) is used to relate stress state to plastic slip rates on each slip system such that

$$\dot{\gamma}_k = \dot{\gamma}_0 sgn(\tau^{(\kappa)})\left[\frac{\varsigma^{(\kappa)}}{g^{(\kappa)}}\right]^m, \tag{8}$$

where $g^{(\alpha)}$ characterizes the strength of each slip system and is a functional of all past slip history and $\dot{\gamma}_0$ is a reference strain rate. We choose a large value of m in the simulation so that the plastic constitutive formulation becomes almost rate-independent and $g^{(\alpha)}$ can be interpreted as the critical resolved shear stress of the κth slip system, i.e. a significant slip occurs only on those slip systems for which $\varsigma^{(\alpha)}$ is approximately equal to $g^{(\kappa)}$. Peirce et al. (1983) first used such a rate-dependent formulation in the context of single crystal plasticity computations, as discussed by Pan and Rice (1983).

4. Finite element formulation

In order to solve boundary value problems incrementally, the equations must be discretized. A commercial software ABAQUS/Standard version 6.6.1 is used for the finite element simulation with a user-material (UMAT) subroutine for single crystal plasticity written by Huang (1991). The formulation in the UMAT follows that of Asaro and Rice (1977), Asaro (1983). Although the theory discussed above assumes infinitesimal deformation gradients (i.e. small strain and small rotations) the UMAT and the simulations discussed herein account rigorously for the effects of a finite deformation gradient. The time integration scheme implemented in the UMAT is the tangent modulus method Peirce et al. (1984) for rate dependent solids. Following Kanchi et al. (1978) the increment in plastic slip $\gamma^{(\kappa)}$ on the κth slip system during a time increment Δt is

$$\Delta\gamma^{(\kappa)} = \left[(1-\theta)\dot{\gamma}_t^{(\kappa)} + \theta\dot{\gamma}_{t+\Delta t}^{(\kappa)}\right]\Delta t, \tag{9}$$

where the interpolation parameter, θ, is chosen to be *0.5* following the recommendation of Peirce et al. (1984). Upon expanding in a Taylor series, the strain rate is written as

$$\dot{\gamma}_{t+\Delta t}^{(\kappa)} = \dot{\gamma}_t^{(\kappa)} + \left[\frac{\partial\dot{\gamma}^{(\kappa)}}{\partial\tau^{(\kappa)}}\right]\Delta\tau^{(\kappa)} + \left[\frac{\partial\dot{\gamma}^{(\kappa)}}{\partial g^{(\kappa)}}\right]\Delta g^{(\kappa)}. \tag{10}$$

The expression for $\Delta\sigma_{ij}$ is obtained by substituting Eqs. 5, 6, 8, 9, and 10, into Eq. (7), whereupon the material Jacobian matrix, $\partial\sigma_{ij}/\partial\varepsilon_{kl}$, which is necessary for the iterative Newton–Raphson solution process, is obtained.

These equations, along with the constitutive hardening models, are implemented numerically within the UMAT. At the end of each solution increment, ABAQUS passes to the UMAT the strain increment, time increment, stress state, and the solution-dependent state variables ($\gamma^{(\kappa)}, g^{(\kappa)}, s_i^{(\kappa)}, m_i^{(\kappa)}, \gamma$, etc.). The UMAT updates the stress state and the solution dependent state variables, and calculates the material Jacobian matrix, $\partial\sigma_{ij}/\partial\varepsilon_{kl}$, and then passes the results to ABAQUS, which then applies the next load increment and calculates the new strain increment via the iterative Newton–Raphson method. This process is iterated until the simulation is completed.

The mesh is shown in Fig. 4a. As illustrated in Fig. 4b, we model only the right half of the material and the wedge indenter. The mesh has fine elements near the tip of the indenter; there are 200 × 160 elements in region *adeb*, 200 × 20 elements in *dghe*, 200 × 20 elements in *gjkh*, 60 × 160 elements in *befc*, 60 × 20 elements in *ehif*, and 60 × 20 elements in *hkli* in Fig. 4b. More detailed images of the mesh are shown in Fig. 4c and Fig. 4d.

In this simulation, the orientation of the crystal is taken to be that shown in Fig. 2a. The function $g^{(\kappa)}$ is taken to be the same for all slip systems and it is maintained constant throughout the simulation in order to model the ideally-plastic properties assumed in the analytical predictions. The critical resolved shear stress on each slip system is denoted as τ. Other parameters used in the simulation include: $\dot{\gamma}_0 = 10^{-3}s^{-1}$, and $m = 50$. The elastic moduli are set as C_{11} = 108.2 GPa, C_{12} = 61.3 GPa, and C_{44} = 28.5 GPa to represent an aluminum single crystal which behaves isotropically to a very good approximation. In order to prevent the propagation of singular zero energy hourglass modes, we introduce a small (between 0.3% and 0.5% of the elastic shear modulus) artificial hourglass stiffness. The element type used in the simulation is plane strain first-order 4-node quadrilaterals that use selectively reduced integration along with a hybrid formulation. Further details of methods and procedures can be found in Kysar (2001a) and Kysar (2001b). It is important to note that the single crystal plasticity formulation with the same parameters employed herein has been verified against the analytical solution for stress and deformation state around a cylindrical void in a single crystal (Kysar et al., 2005; Gan et al., 2005).

For boundary conditions (cf. Fig. 4b), the displacement in the x_1-direction, denoted as u_1, is constrained to be zero on line *aj*, and the displacement, u_2, in the x_2-direction is constrained to be zero on line *jl*. The wedge indenter is modeled as a rigid surface oriented at an angle ϕ relative to the upper surface of the mesh. The rigid surface moves down into the mesh as a linear function of time during the simulation. We invoke the 'small-sliding' approximation since a point contacting a surface is not expected to slide more than an element dimension. The coefficient of friction between the two surfaces is set to zero to model frictionless indentation.

The output from the finite elements simulations will be plotted in two different forms. One will be contour plots of field quantities in the deformed configuration shown in Fig. 5 where the rigid indenter has penetrated the material so that the contact point singularity is at distance a from the antisymmetry boundary. The position of the contact point singularity is marked by a small black circle in each of the contour plots. The other will be to plot field quantities on circular arcs of different radii ($r_0 = 0.1a, r_1 = 0.2a, r_2 = 0.3a$, and $r_3 = 0.4a$) from the contact point singularity as shown in Fig. 5. In this way, the presence of an asymptotic behavior (i.e. behavior independent of distance from contact point singularity) can be evaluated and, where it exists, the extent of the asymptotic region can be determined. All stress quantities are normalized relative to the critical resolved shear stress τ.

It is known (Drugan and Rice, 1984 and Drugan, 1986) that stresses cannot change discontinuously across a surface that propagates quasistatically through an elastic–plastic material of the kind modeled in this study. Therefore, we first

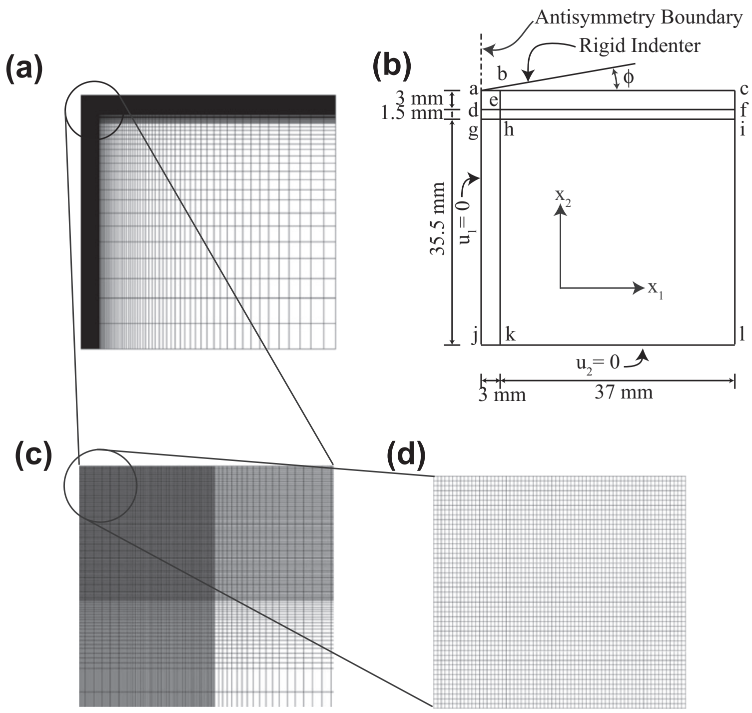

Fig. 4. Mesh detail of finite element simulation: (a) overall mesh; (b) schematic representation showing various regions of mesh along with the indenter surface; (c) close-up view of mesh; and, (d) region of mesh penetrated by indenter surface.

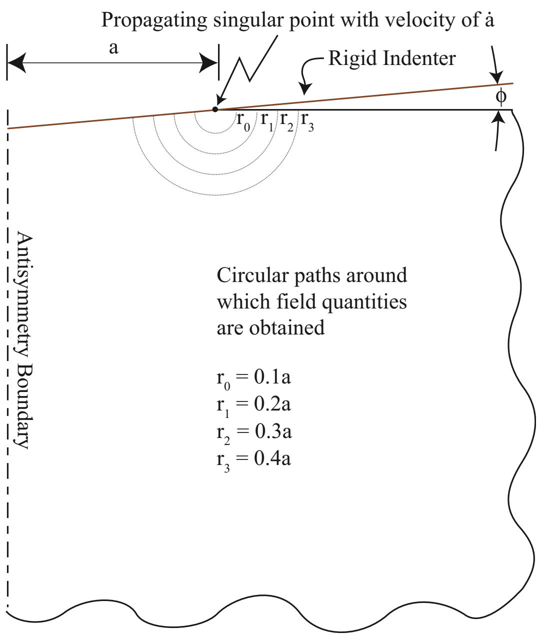

Fig. 5. Circular paths along which field quantities are reported, where a is the distance of the contact point singularity from the antisymmetry boundary, and $\dot{a}$ is the rate of motion of contact point singularity with respect to time. Radii of paths are $r_0 = 0.1a$, $r_1 = 0.2a$, $r_2 = 0.3a$, and $r_3 = 0.4a$.

performed a numerical convergence study to ensure that the stress fields near the moving contact point singularity do not exhibit any discontinuous behavior. The results of the convergence study are shown in Fig. 6, where nearly-flat wedge indenters with several different included angles are employed while maintaining the same vertical penetration rate of the rigid indenter into the mesh. The transition of the stress component σ_{12} with varying angle ϕ (cf. Fig. 4b) is instructive with regard to whether a stress discontinuity exists. With sufficiently small values of ϕ, (i.e. $\phi = 0.0191°$ and $\phi = 0.0382°$ for which the

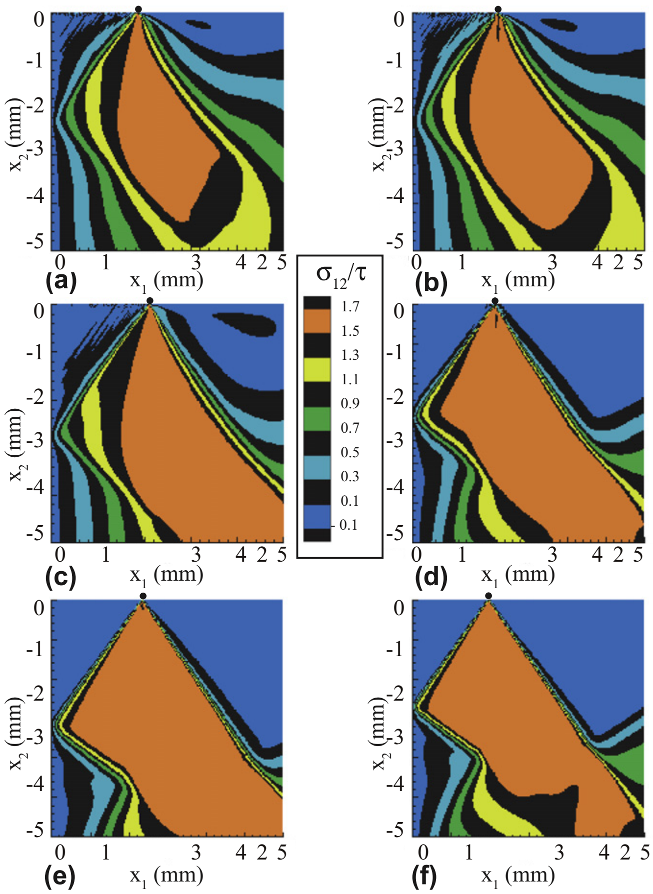

Fig. 6. The σ_{12} stress field transition for different ϕ: (a) $\phi = 0.0191°$; (b) $\phi = 0.0382°$; (c) $\phi = 0.0764°$; (d) $\phi = 0.1528°$; (e) $\phi = 0.3056°$; and (f) $\phi = 0.6112°$. The instantaneous position of the contact point singularity is indicated by a small circle in each plot.

contact point singularity propagates two and one element lengths, respectively, each time increment) it is clear that σ_{12} is continuous over the entire domain as seen in Figs. 6a and b. To demonstrate convergence, we note that essentially the same solution is predicted when values of ϕ are chosen such that the contact point singularity propagates 3/2, 5/4, π/e, $\pi/3$, $3/\pi$, and e/π of an element length, respectively, per time increment, while the maximum time increment remains the same for each value of ϕ. Also, the same σ_{12} field results for a series of simulations when the maximum time increment is varied for constant values of ϕ. In addition, the solution is stable for values of θ in Eq. (9) ranging from 0.5 to 1. We will show that this field corresponds to the analytical predictions of the asymptotic stress and deformation fields of the contact point singularity associated with quasistatic impingement of the nearly-flat wedge indenter into the material.

On the other hand, when ϕ is set to larger values such as $\phi = 0.0764°$, $\phi = 0.1528°$, $\phi = 0.3056°$, and $\phi = 0.6112°$ as shown in the remaining subplots of Fig. 6, it is evident that the structure of the σ_{12} field changes dramatically and very rapid variations in σ_{12} are evident. For the two largest values of ϕ (i.e. $\phi = 0.3056°$, and $\phi = 0.6112°$), the σ_{12} field converges to a solution that contains discontinuities at $\theta = -54.7°$ and $\theta = -125.3°$ and the value of σ_{12} remains relatively constant within the angular sectors. This solution is also stable for values of θ in Eq. (9) ranging from 0.5 to 1. Given the discontinuous changes in σ_{12}, this solution is not valid for the problem under consideration, but rather corresponds to the solution for a flat punch. We do not attempt to address here the reasons that lead the numerical solutions to converge to the discontinuous solution for the larger values of ϕ.

Henceforth we will limit our discussion to the solution for the contact point singularity with continuous stresses for which the included angle of the nearly-flat wedge indenter is 179.92° (i.e. $\phi = 0.0382°$) corresponding to the case of Fig. 6b.

5. Simulation results for nearly-flat wedge indentation

In order to investigate in detail the fields associated with the quasistatically moving contact point singularity, a total of 200 increments is performed in the simulation at which time the contact point singularity has passed about 120 elements on

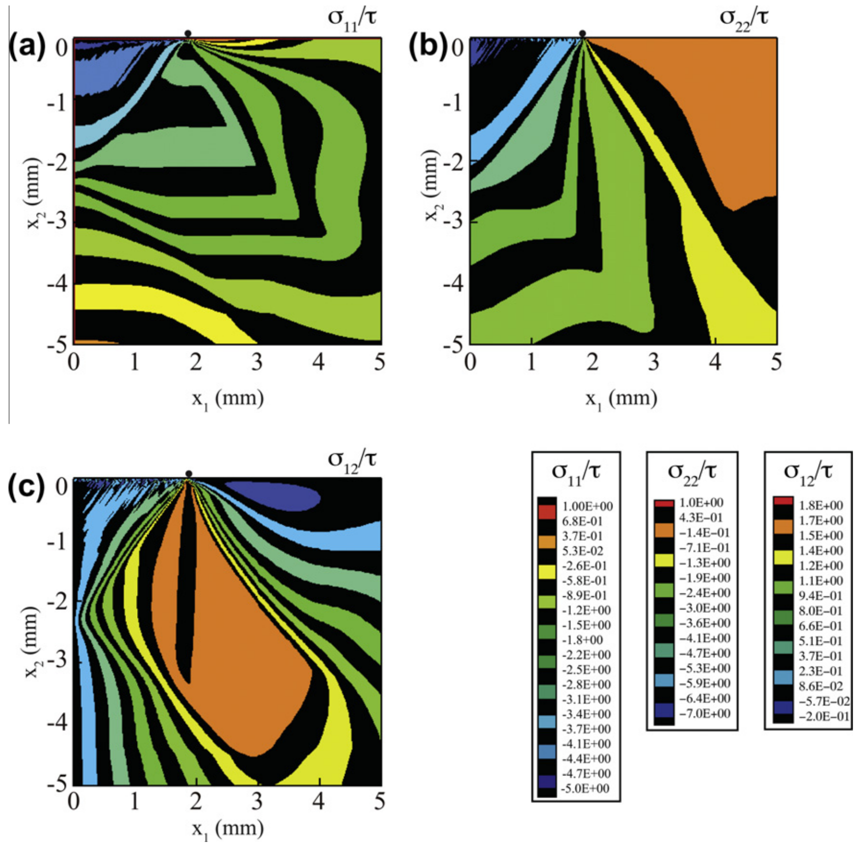

Fig. 7. Contours of stress components associated with quasistatically propagating contact point singularity: (a) σ_{11}/τ; (b) σ_{22}/τ; and, (c) σ_{12}/τ. The instantaneous position of the contact point singularity is indicated by a small circle in each plot.

line *ab* of Fig. 4b. The field quantities of stresses, slip increments, velocities, and lattice rotation are presented as contour plots and also as a function of angle at various radii around the contact point singularity.

5.1. Stresses

The contours of the in-plane stress components are plotted in Fig. 7, where it is evident that all stress components are continuous throughout the domain, although there is some numerical noise under the contact region of the wedge indenter. In the immediate vicinity of the contact point singularity, the contour boundaries appear to be approximately radial with respect to the contact point singularity. This suggests that, asymptotically, the stress state is approximately independent of radius from the contact point singularity. Fig. 8 shows each of the normalized stress components taken along the different circular arcs shown in Fig. 5. The vertical dashed lines indicate the angles of the boundaries that divide elastic sectors I, II, III, and IV shown in Fig. 2b. In accordance with the predicted asymptotic behavior (and in spite of the numerical noise present in the data), it is clear that the stresses do not depend systematically on radius. In addition, the numerical results for stress distribution in Fig. 8 are very similar to the predicted distribution in Fig. 3b.

With regard to the angular distributions of the stresses in Figs. 8 and 3b, σ_{12}/τ and σ_{22}/τ are zero at $\theta = 0°$ as required by the boundary conditions; also $\sigma_{12} = 0$ at $\theta = -180°$ since the indenter is frictionless. The value of σ_{12}/τ reaches its maximum value at $\theta = -90°$ where kink-type deformation on slip system (ii) is expected to occur. The stresses σ_{11}/τ and σ_{22}/τ reach almost the same normalized stress value of between -5 and -6 at $\theta = -180°$, which indicates a high degree of stress triaxiality that inhibits plastic deformation from occurring under the indenter.

The stresses along different circular arcs at various radii from the contact point singularity are plotted in stress space in Fig. 9; these results also confirm the asymptotic nature of the solution since there is no systematic change with radius. Referring specifically to Fig. 9a, the stress trajectory starts very near the center of the yield surface at $\theta = 0°$ in the physical domain, so that $\sigma_{12}/\tau = 0$ and $\sigma_{11}/\tau = \sigma_{22}/\tau$, indicating the stress states to be elastic. As θ decreases to $\theta = -54.7°$ within elastic sector I in Fig. 2b, the trajectory proceeds clockwise in Fig. 9a and touches a line segment of the yield surface tangentially activating the slip system (iii). From $\theta = -54.7°$, the stress trajectory enters elastic sector II until it touches tangentially the top line segment of the yield surface activating slip system (ii). The stress trajectory then continues into elastic sector III until it reaches

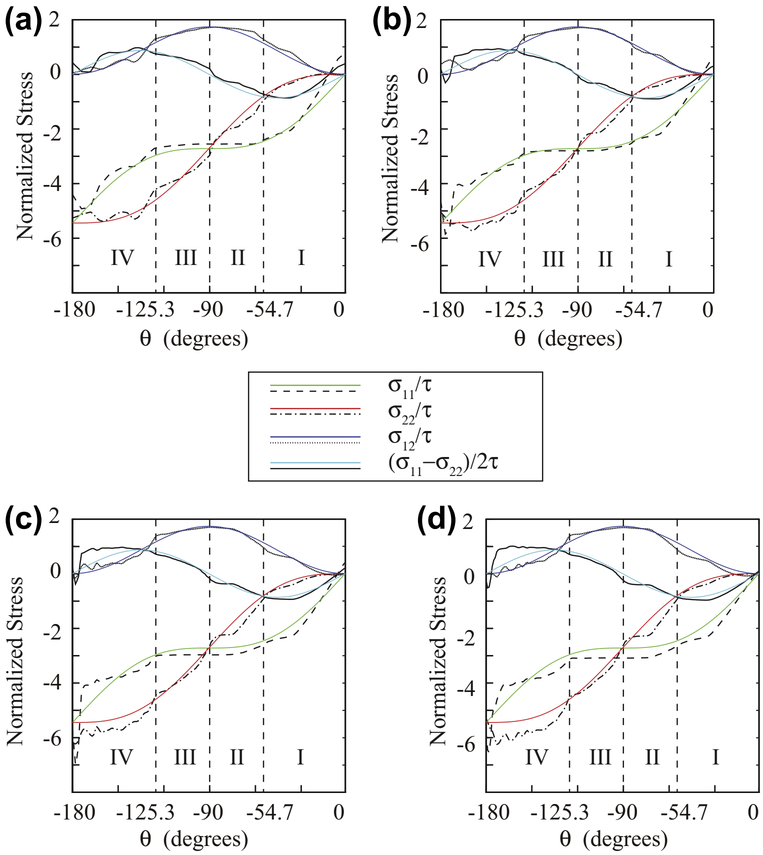

Fig. 8. Stress components as a function of angle and radius with respect to the contact point singularity: (a) $r_0 = 0.1a$; (b) $r_1 = 0.2a$; (c) $r_2 = 0.3a$; and, (d) $r_3 = 0.4a$. Colored lines indicate analytical predictions and black lines indicate numerical results.

the upper right side line segment of the yield surface activating the slip system (i) at $\theta = -125.3°$ of the physical domain. Then, the trajectory goes back to near the origin of stress space where the stress state is elastic within elastic sector IV. The last segment shows slightly different behaviors on different circular paths due to the numerical errors where elements experienced significant deformation under the wedge indenter as the singular point passed.

5.2. Slip increments

Fig. 10 shows increments of plastic slip that occur during a small increment of movement of the contact point singularity to the right. The plastic slip increment is normalized to obtain the dimensionless quantity $\dot{\gamma}^{(\kappa)}a/\dot{a}$. Three rays of plastic slip increment emanate from the contact point singularity. From Fig. 10a and Fig. 2a, it is clear that concentrated glide shear on slip system (i) occurs at $\theta = -125.3°$ because the orientation of the concentrated slip in Fig. 10a is on the line parallel to slip system (i) that emanates from the contact point singularity. Similarly, from Fig. 10b, it is apparent that a concentrated kink-shear due to the slip system (ii) occurs on $\theta = -90.0°$ because the orientation of the concentrated slip coincides with the normal to slip system (ii) that emanates from contact point singularity. Also, concentrated glide shear on slip system (iii) occurs at $\theta = -54.7°$, as evident from Fig. 10c.

The sum of the three slip increments is shown in Fig. 10d which also indicates four characteristic points of the slip increment field labeled as **A**, **B**, **C** and **D**. Point **A** coincides with the contact point singularity. The glide shear ray on slip system (i) begins as point **A** and reaches the line of antisymmetry at point **B**. Then, interestingly, another ray of slip increment due to kink-shear on the slip system (i) emanates from point **B** along the normal direction to slip system (i). At point **C** it meets the kink-shear ray on slip system (ii) that emanates from point **A**. The path traversed through the material by point **C** from the beginning of the indentation process to the current time in the simulation is indicated by the white line from point **O** at the origin to point **C** in Fig. 10d. Taking into account the orientations of the active slip systems and assuming infinitesimal deformations, the line **OC** ideally is oriented at $-64.7°$ relative to the upper surface of the crystal. The significance of line **OC** is that the material below it has suffered plastic deformation only from slip system (i). Above line **OC**, plastic deformation at a material point will be activated sequentially and individually by all three slip systems as the contact point singularity propagates to the right. From the antisymmetric nature of this problem, slip system (iii) is the only slip system that is activated under

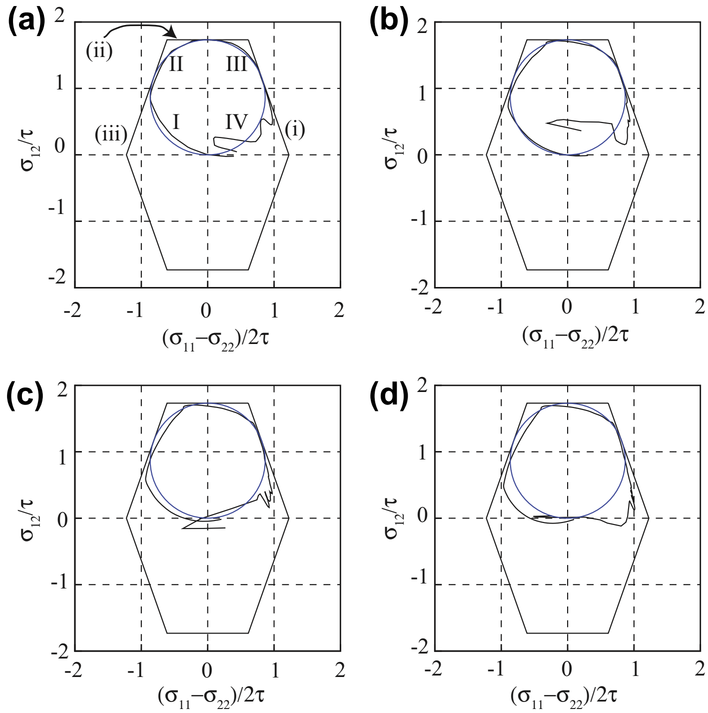

Fig. 9. Stress trajectories in vicinity of contact point singularity for various radii: (a) $r_0 = 0.1a$; (b) $r_1 = 0.2a$; (c) $r_2 = 0.3a$; and, (d) $r_3 = 0.4a$. Blue lines indicate analytical predictions and black lines indicate numerical results.

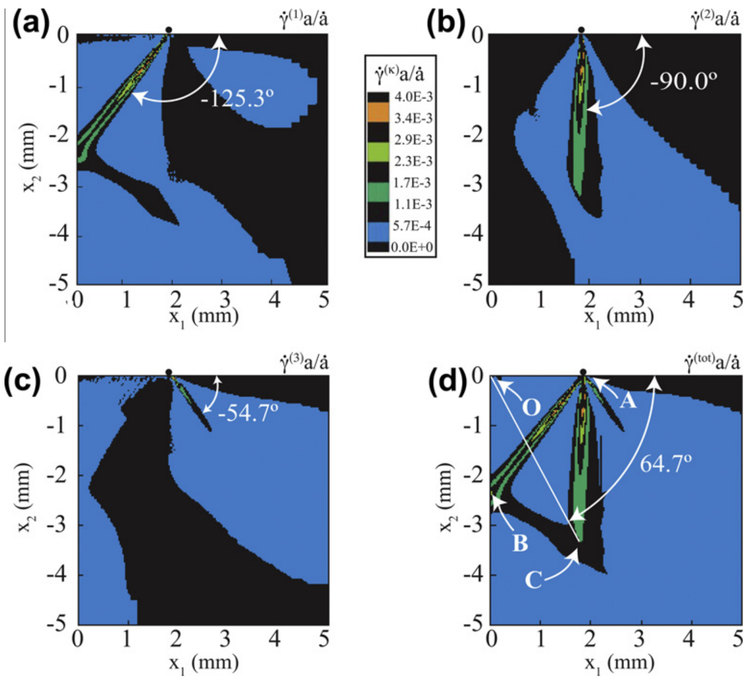

Fig. 10. Normalized slip increments $\dot{\gamma}^{(\kappa)}a/\dot{a}$ on: (a) slip system (i); (b) slip system (ii); (c) slip system (iii); (d) sum of slip increments on three effective in-plane slip systems, where characteristic points of the slip increment field are indicated.

the reflection of line **OC** about the antisymmetry axis on the left side of the domain. Hence, both slip system (i) as well as slip system (iii) are expected to contribute to plastic deformation that occurs directly on the antisymmetry boundary. From another perspective, slip system (ii) is not expected to be activated on the antisymmetry boundary because $\sigma_{12} = 0$. Thus, dislocations from slip system (i) and slip system (iii) are expected to create a wall of dislocations along the antisymmetry boundary as point **B** moves downward into the crystal during indentation.

Plastic slip increments along circular arcs around the contact point singularity are shown in Fig. 11 for different radii. The slip increments occur predominantly in the special directions shown in Fig. 10 that correspond to the sector boundaries in Fig. 2b; the active slip systems at each sector boundary are in accord with the analytical predictions. In addition, Fig. 11 shows that the plastic slip increments reduce to a negligible magnitude in the regions between the sector boundaries, so that the material in the sectors themselves undergoes predominantly elastic deformation. Finally, Fig. 11 demonstrates that the magnitude of the slip increments decreases with distance from the contact point singularity.

5.3. Velocity fields

While there can be no discontinuities of stress associated with the quasistatically propagating contact point singularity, discontinuities in velocity are admissible (Drugan and Rice, 1984; Drugan, 1986). Fig. 12 shows the velocity fields normalized by $\dot{a}$. Rapid variations in $v_1/\dot{a}$ are seen at angles $\theta = -54.7°$ and $\theta = -125.3°$ relative to the contact point singularity that coincide, respectively, with glide shear rays on slip system (iii) and (i), respectively. Fig. 12 shows there to be a rapid change in $v_1/\dot{a}$ that extends from point **B** to point **C**. In addition, the contour boundaries of velocity emanate radially from points **A** and **B** to a very good approximation, as expected for an asymptotic field.

The distributions of the normalized velocities on circular arcs around the contact point singularity are shown for different radii in Fig. 13, where it is clear that the velocities vary only slightly with radius. The value of $v_2/\dot{a}$ change distinctly at each of the three sector boundaries, whereas the value of $v_1/\dot{a}$ changes distinctly at the boundary between sectors I and II and between sectors III and IV, but not at the boundary between sector II and III. Both velocities are approximately constant within the sectors, which indicates that the velocities due to elastic deformation within the sectors is very small as compared to the velocities induced by plastic deformation in the sector boundaries. Velocity discontinuities are allowable in radial directions from the contact point singularity but velocity discontinuities in the circumferential direction are not admissible. In Fig. 13, the radial component of the velocity, $v_r/\dot{a}$, changes distinctly at each of the sector boundaries; however the circumferential velocity component, $v_\theta/\dot{a}$, is continuous for all θ.

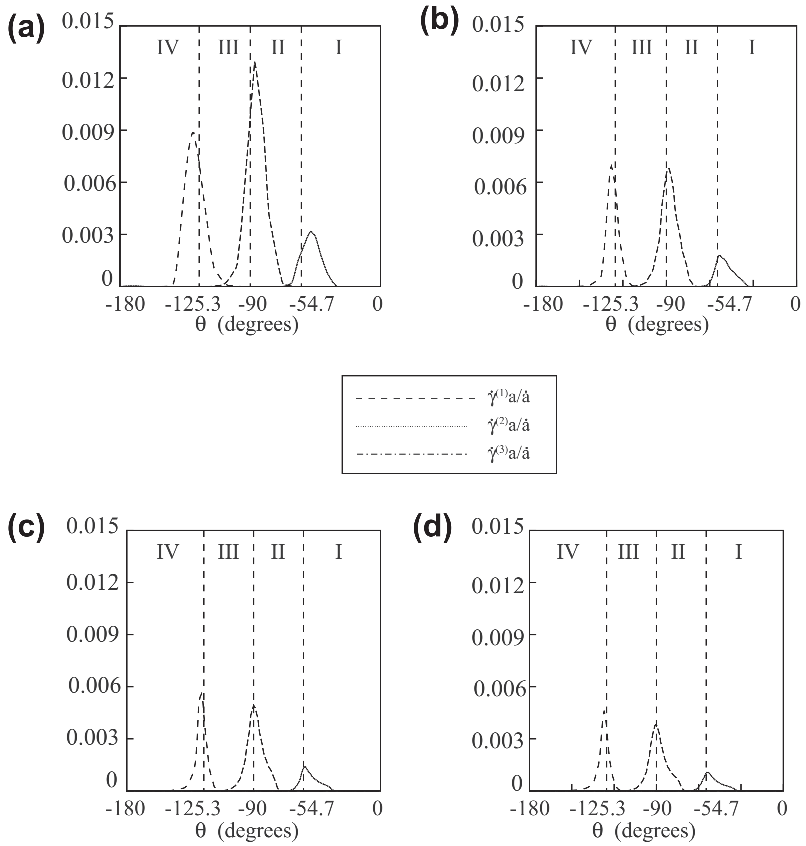

Fig. 11. Slip increments as a function of angle and radius with respect to the contact point singularity: (a) $r_0 = 0.1a$; (b) $r_1 = 0.2a$; (c) $r_2 = 0.3a$; and, (d) $r_3 = 0.4a$.

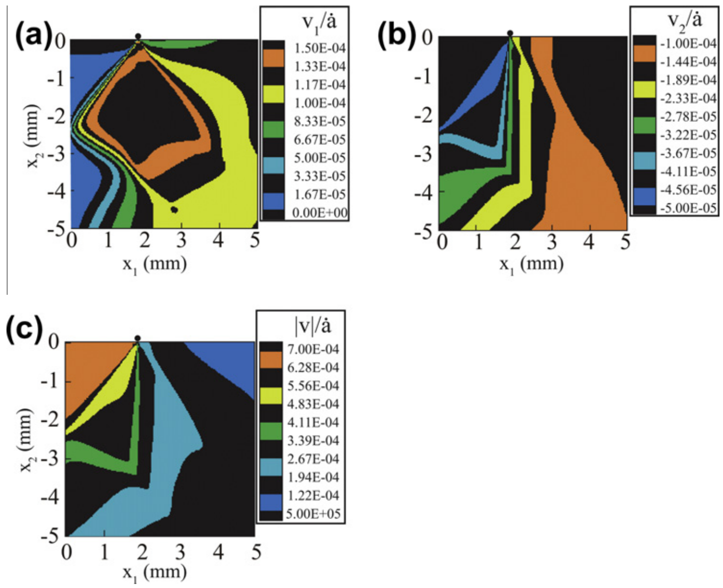

Fig. 12. Normalized velocity fields: (a) $v_1/\dot{a}$; (b) $v_2/\dot{a}$; and, (c) $|v|/\dot{a}$.

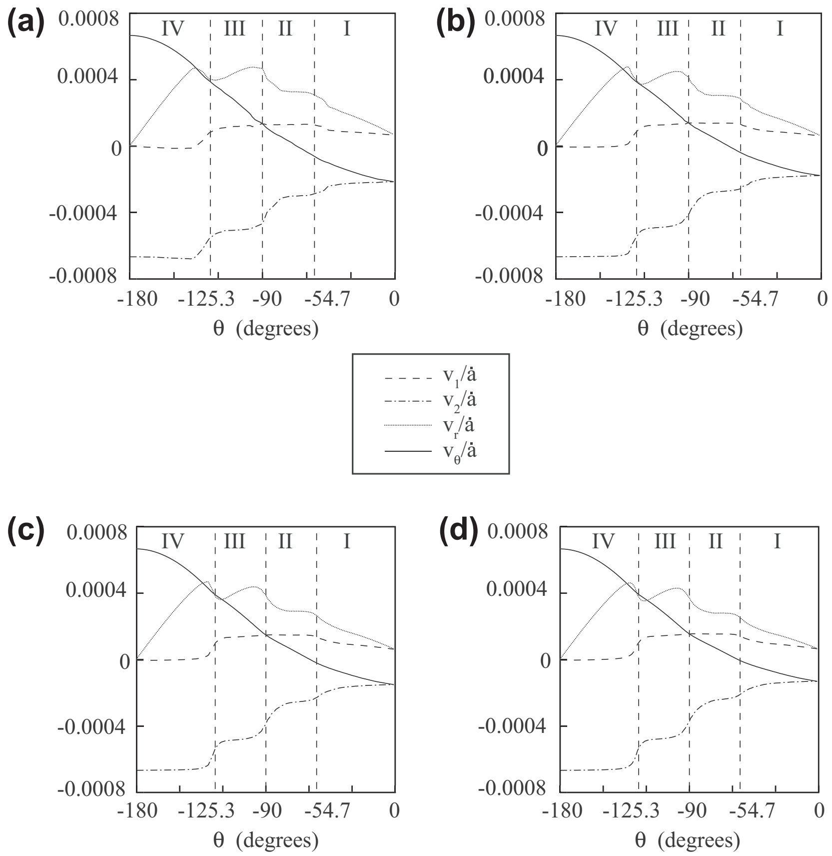

Fig. 13. Normalized velocities as a function of angle and radius with respect to the contact point singularity: (a) $r_0 = 0.1a$; (b) $r_1 = 0.2a$; (c) $r_2 = 0.3a$; and, (d) $r_3 = 0.4a$.

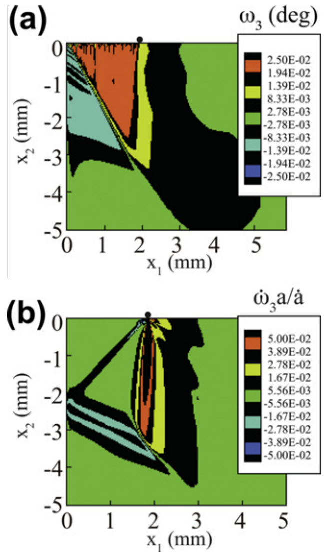

Fig. 14. Rotation of crystal lattice: (a) lattice rotation in degrees; (b) normalized lattice rotation rate, $\dot{\omega}_3 a/\dot{a}$.

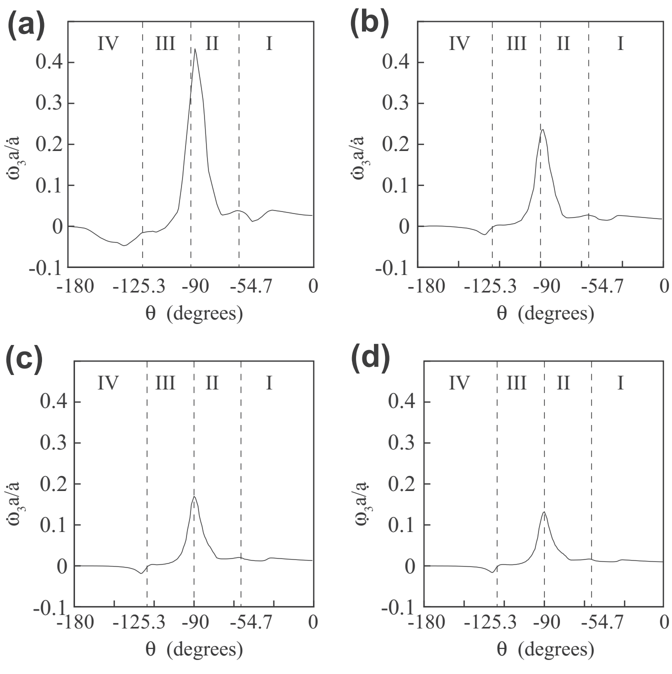

Fig. 15. Normalized lattice rotation rates, $\dot{\omega}_3 a/\dot{a}$, as a function of angle and radius with respect to the contact point singularity: (a) $r_0 = 0.1a$; (b) $r_1 = 0.2a$; (c) $r_2 = 0.3a$; and, (d) $r_3 = 0.4a$.

5.4. Lattice rotation

The crystal lattice rotates as a consequence of plastic slip. Given that a two-dimensional deformation state is induced in the crystal, the only non-zero component of lattice rotation, denoted as ω_3, is about the x_3-axis (cf. Fig. 2b) where a positive rotation is defined as counterclockwise. Contours of lattice rotation and lattice rotation rate (normalized as $\dot{\omega}_3 a/\dot{a}$) are shown in Figs. 14a and b, respectively. Below line **OC** (cf. Fig. 10d) the lattice rotation is negative and the kink-shear on slip system (i) that coincides with line **BC** contributes the majority of the lattice rotation. Above line **OC** the lattice rotation is positive and the kink-shear on slip system (ii) on line **AC** contributes the majority of the lattice rotation. Thus the total lattice rotation changes sign across line **OC**. This conclusion is reinforced by the distribution of lattice rotation rate in Fig. 14b,

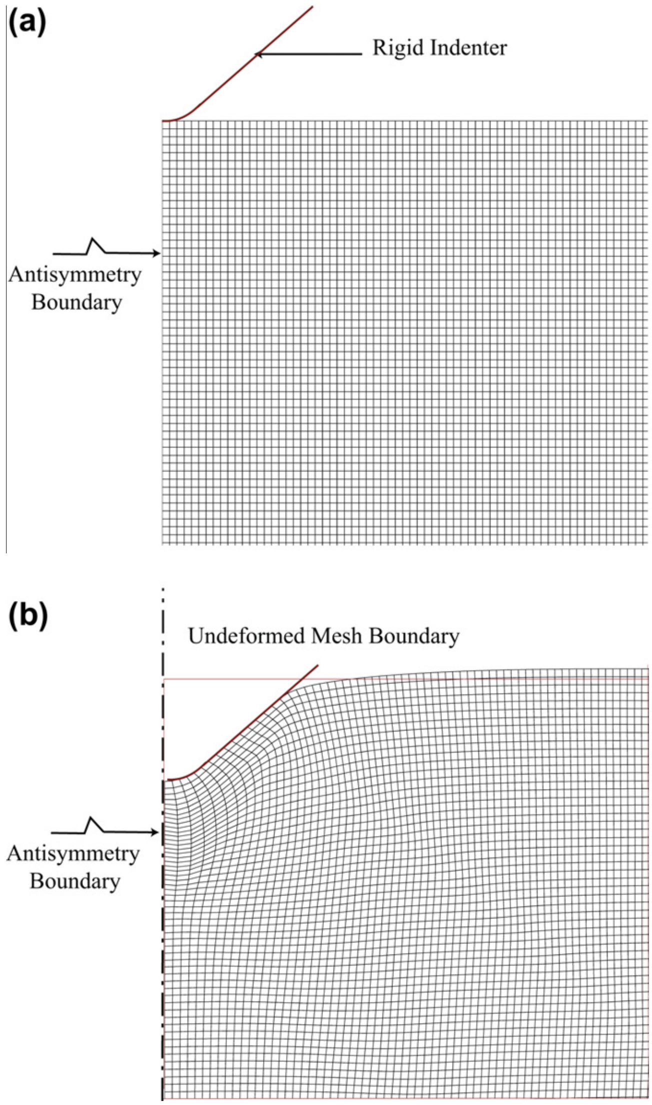

Fig. 16. Finite element mesh for wedge indentation with 90° included angle: (a) Geometry of mesh and rigid indenter; (b) Deformed mesh after indentation to depth of 250 μm.

where the structure of the field is consistent with the structure of the total slip increment field in Fig. 10d. Fig. 15 shows the variation of lattice rotation rates on circular arcs at different radii from the contact point singularity. The results also demonstrate how the lattice rotation rate diminishes with distance from the contact point singularity.

6. Simulation results for 90° wedge indentation

In order to investigate the effect of finite deformations and lattice rotations, we compare wedge indentation simulations (Kysar et al., 2010) using a 90° included angle rigid indenter (with a slight radius of curvature at the tip) to the results using a nearly-flat wedge. The mesh near the indented region is shown in Fig. 16a prior to deformation. The simulation procedures employed were identical to those described in Section 4 except that the material is assumed to be a nickel single crystal rather than an aluminum single crystal. Thus, the only difference is the elastic properties; the orientation of the crystal as well as the plastic properties are the same for both the nearly-flat wedge simulation and the 90° angle wedge simulation. Fig. 16b shows the mesh after 250 μm of indentation. Only the right half of the domain needs to be modeled.

The normalized plastic slip increments on individual slip systems are shown in Fig. 17. We first recall that the deformation fields under the nearly-flat wedge show a kink-shear band on slip system (i) that coincides with line **BC** of Fig. 10d. This feature persists to the case of the deformation field under the 90° wedge indenter as seen in Fig. 17a where concentrated glide shear on slip system (i) emanates from the contact point singularity and extends down toward the antisymmetry

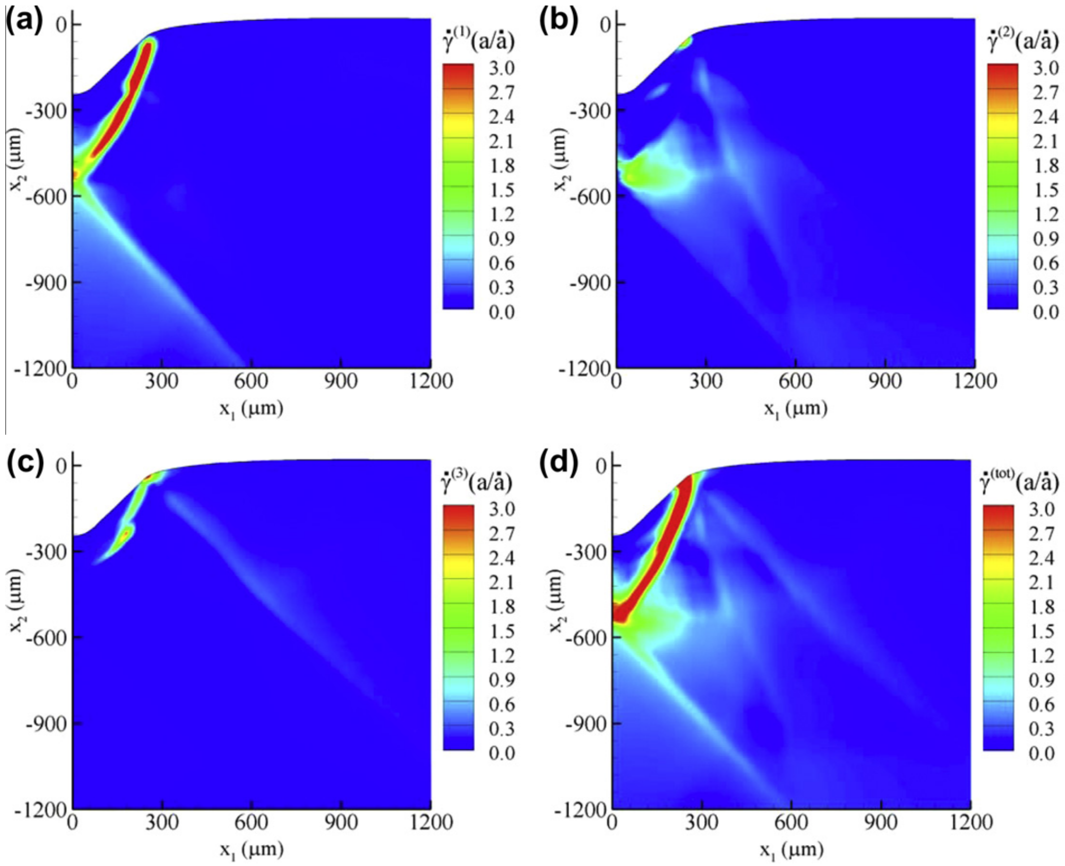

Fig. 17. Increment of plastic slip, $\dot{\gamma}^{(\kappa)}a/\dot{a}$, on effective in-plane slip systems: (a) Slip System (i); (b) Slip System (ii); (c) Slip System (iii); (d) Total from all slip systems.

boundary along the local $\mathbf{S}^{(1)}$ direction from which concentrated kink-shear is activated and extends down and away from the antisymmetry line in the direction of the local $\mathbf{N}^{(1)}$. Thus the distribution of $\dot{\gamma}^{(1)}a/\dot{a}$ is analogous to that for the case of the nearly-flat wedge, as seen in Fig. 10a; the only difference is that slip system (i) in Fig. 17a has obviously rotated and deformed relative to the nearly-flat case. The concentrated kink-shear that extends down and away from the antisymmetry line is seen experimentally in Fig. 7a of Kysar et al. (2010) in the form of spatial variations of GND densities on slip system (i) that coincide with local direction $\mathbf{N}^{(1)}$ in the deformed configuration. Thus, the existence of the predicted kink-shear bands is experimentally validated.

The distribution of $\dot{\gamma}^{(2)}a/\dot{a}$ in Fig. 17b is significantly different than that in Fig. 10b. For the case of the nearly-flat wedge, a concentrated kink-shear originates from the contact point singularity, whereas for the 90° wedge the concentrated kink-shear from the contact point singularity is much diminished. Another significant difference is that for the 90° wedge, slip system (ii) is activated at the point where concentrated glide shear on slip system (i) meets the antisymmetry boundary. Slip system (ii) is not activated at the antisymmetry boundary for the nearly-flat wedge because the resolved shear stress on slip system (ii) is zero (since the antisymmetry boundary requires $\sigma_{12} = 0$ and $\mathbf{S}^{(2)}$ is originally horizontal and remains essentially horizontal throughout the infinitesimal deformation of a nearly-flat wedge indentation). However the resolved shear stress on slip system (ii) becomes non-zero as the crystal rotates due to plastic deformation on slip system (i) during the 90° wedge indentation.

Fig. 17c shows the distribution of $\dot{\gamma}^{(3)}a/\dot{a}$. A concentrated glide shear originates from the contact point singularity and extends along the local $\mathbf{S}^{(3)}$ direction; this also exists for the case of the nearly-flat indentation (cf. Fig. 10c). In fact, the slip activity extends further into the material for the 90° wedge than it does for the nearly-flat wedge. The finite deformation and rotations induced under the 90° wedge activates slip system (iii) immediately under the indenter; however the slip activity does not extend all the way to the antisymmetry boundary. The analog of this slip activity for the nearly-flat wedge is completely absent.

The distribution of the total slip increment, $\dot{\gamma}^{(tot)}a/\dot{a}$, from all three effective slip systems is shown in Fig. 17d. All the slip increment features in the slip increment fields for the nearly-flat wedge shown in Fig. 10b persist as the included angle of the indenter is reduced from essentially 180° to 90°, although the relative magnitudes and extents of plastic slip increment within the domains may vary. The only substantial difference in the slip increment fields is that slip system (ii) is activated at the antisymmetry boundary due to the effects of finite rotations under the 90° indenter, whereas it is not for the case of the nearly-flat wedge. Thus, we conclude that both slip systems (i) and (ii) are activated in the region under the 90° tip, near and to the right of the antisymmetry boundary whereas only slip system (i) is active in that region for the case of the nearly-flat wedge. As a consequence, the dislocation structure is expected to consist of dislocations from slip systems (i) and (ii) on the right of the antisymmetry boundary and is expected to consist of dislocations from slip systems (i) and (iii) immediately to the left of the antisymmetry boundary. The experimental measurements of the GND densities in Figs. 7 and 8 of Kysar et al. (2010) bear out these predictions, both with regard to the existence as well as the signs of the GND densities on the pertinent slip systems.

7. Conclusion

Finite element simulations of nearly-flat wedge indentation into elastic, ideally-plastic face-centered cubic (FCC) crystals under plane strain conditions are performed. The included angle of the indenter was chosen to be 179.92° degrees so that the resulting plastic deformation induces a negligible amount of lattice rotation. The stresses, velocities, slip increments, lattice rotation, and lattice rotation rates of the fields for the quasistatically moving contact point singularity are all consistent with the predicted asymptotic fields based on an analytical model by Saito and Kysar (2011). Specifically, sufficiently close to the contact point singularity the asymptotic fields vary only with angle. The fields consist of four angular sectors that instantaneously undergo elastic deformation; however instantaneous plastic deformation is induced at the boundaries between the sectors. The stresses are continuous with angle, but there are rapid variations in the radial component of velocity relative to the contact point singularity, consistent with known requirements for interior surfaces of deformation that propagate through a general class of elastic–plastic materials. Finally, the stress distribution as a function of angular position as well as the trajectory of the stresses in stress space are in close accordance with the analytical predictions.

In addition, simulations are performed for a wedge indenter with a 90° included angle in order to investigate the consequences of finite deformation and finite lattice rotation. The salient features of the deformation fields for the nearly-flat indenter persist in the deformation fields for the 90° wedge indenter. The main effect of the finite lattice rotation is to cause a second slip system to be activated at the antisymmetry boundary, which is consistent with experimental measurements of GND densities (Kysar et al., 2010). One other characteristic feature of the deformation fields in the numerical predictions is a concentrated kink-shear deformation that emanates from the antisymmetry boundary; such features are consistent with experimental measurements of GND density structures (Kysar et al., 2010).

Acknowledgments

Support from the Air Force Office of Scientific Research (FA9550-09-1-0048), Lawrence Livermore National Laboratory (B585562) and NSF (DMR-0706058) is gratefully acknowledged. The authors thank W. J. Drugan, E. Busso, C. Niordson, and an anonymous reviewer for enlightening discussions.

References

Asaro, R.J., 1983. Micromechanics of crystals and polycrystals. Advances in Applied Mechanics 23, 1–114.
Asaro, R.J., Rice, J.R., 1977. Strain localization in ductile single crystals. Journal of the Mechanics and Physics of Solids 25 (5), 309–338.
Drugan, W.J., 1986. A more direct and general-analysis of moving strong discontinuity surfaces in quasi-statically deforming elastic–plastic solids. Journal of Applied Mechanics 53 (1), 224–226.
Drugan, W.J., 2001. Asymptotic solutions for tensile crack tip fields without kink-type shear bands in elastic-ideally plastic single crystals. Journal of the Mechanics and Physics of Solids 49 (9), 2155–2176.
Drugan, W.J., Rice, J.R., 1984. Restrictions on quasi-statically moving surfaces of strong discontinuity in elastic–plastic solids. In: Dvorak, G.J., Shield, R.T. (Eds.), Mechanics of Material Behavior (The D.C. Drucker Anniversary Volume). Elsevier, pp. 59–73.
Drugan, W.J., Rice, J.R., Sham, T.L., 1982. Asymptotic analysis of growing plane-strain tensile cracks in elastic ideally plastic solids. Journal of the Mechanics and Physics of Solids 30 (6), 447–473.
Gan, Y.X., Kysar, J.W., Morse, T.L., 2005. Cylindrical void in a rigid-ideally plastic single crystal II: experiments and simulations. International Journal of Plasticity 22 (1), 39–72.
Havner, K.S., 1992. Finite Plastic Deformation of Crystalline Solids. Cambridge University Press, Cambridge.
Havner, K.S., 1972. On Hill's stress rate in the continuum mechanics of polycrystals. Acta Mechanica 14 (2–3), 183–187.
Havner, K.S., 1973. On the mechanics of crystalline solids. Journal of the Mechanics and Physics of Solids 21 (6), 383–394.
Hill, R., 1966. Generalized constitutive relations for incremental deformation of metal crystals by multislip. Journal of the Mechanics and Physics of Solids 14 (2), 95–102.
Hill, R., Havner, K.S., 1982. Perspectives in the mechanics of elastoplastic crystals. Journal of the Mechanics and Physics of Solids 30 (1–2), 5–22.
Hill, R., Rice, J.R., 1972. Constitutive analysis of elastic–plastic crystals at arbitrary strain. Journal of the Mechanics and Physics of Solids 20 (6), 401–413.
Huang, Y., 1991. A User-material Subroutine Incorporating Single Crystal Plasticity in the ABAQUS Finite Element Program: Mech Report 178. Division of Applied Sciences, Harvard University, Cambridge, Massachusetts 02138.
Huang, Y., 1995. Tensile crack-tip stress-fields in elastic-perfectly plastic crystals. Journal of Applied Mechanics 62 (1), 238–240.
Hutchinson, J.W., 1976. Bounds and self-consistent estimates for creep of polycrystalline materials. Proceedings of the Royal Society of London Series A – Mathematical Physical and Engineering Sciences 348 (1652), 101–127.
Kanchi, M.B., Zienkiewicz, O.C., Owen, D.R.J., 1978. Viscoplastic approach to problems of plasticity and creep involving geometric non-linear effects. International Journal for Numerical Methods in Engineering 12 (1), 169–181.
Kysar, J.W., 2001a. Continuum simulations of directional dependence of crack growth along a copper/sapphire bicrystal interface. Part I: experiments and crystal plasticity background. Journal of the Mechanics and Physics of Solids 49 (5), 1099–1128.

Kysar, J.W., 2001b. Continuum simulations of directional dependence of crack growth along a copper/sapphire bicrystal interface. Part II: crack tip stress/deformation analysis. Journal of the Mechanics and Physics of Solids 49 (5), 1129–1153.
Kysar, J.W., Gan, Y.X., Mendez-Arzuza, G., 2005. Cylindrical void in a rigid-ideally plastic single crystal I: anisotropic slip line theory solution for face-centered cubic crystals. International Journal of Plasticity 21 (8), 1481–1520.
Kysar, J.W., Saito, Y., Oztop, M.S., Lee, D., Huh, W.T., 2010. Experimental lower bounds on geometrically necessary dislocation density. International Journal of Plasticity 26 (8), 1097–1123.
Pan, J., Rice, J.R., 1983. Rate sensitivity of plastic-flow and implications for yield-surface vertices. International Journal of Solids and Structures 19 (11), 973–987.
Peirce, D., Asaro, R.J., Needleman, A., 1983. Material rate dependence and localized deformation in crystalline solids. Acta Metallurgica 31 (12), 1951–1976.
Peirce, D., Shih, C.F., Needleman, A., 1984. A tangent modulus method for rate dependent solids. Computers & Structures 18 (5), 875–887.
Prandtl, L., 1920. Über die härte plastischer körper. Nachtrichten von de Gesellschaft der Wissenschaften zu Göttingen, mathematisch-Physikalische Klasse, 74–85.
Rice, J.R., 1971. Inelastic constitutive relations for solids – an internal-variable theory and its application to metal plasticity. Journal of the Mechanics and Physics of Solids 19 (6), 433–455.
Rice, J.R., 1973. Plane strain slip line theory for anisotropic rigid-plastic materials. Journal of the Mechanics and Physics of Solids 21 (2), 63–74.
Rice, J.R., 1987. Tensile crack tip fields in elastic ideally plastic crystals. Mechanics of Materials 6 (4), 317–335.
Saito, Y., Kysar, J.W., 2011. Wedge indentation into elastic–plastic single crystals, 1: asymptotic fields for nearly-flat wedge. International Journal of Plasticity 27 (10), 1640–1657.
Taylor, G.I., Elam, C.F., 1923. The distortion of an aluminium crystal during a tensile test. Proceedings of the Royal Society of London Series A 102 (719), 643–667.
Zhang, H.W., Huang, Y., 1994. Asymptotic tensile crack-tip stress-fields in elastic-perfectly plastic crystals. International Journal of Fracture 67 (2), 133–142.